Application of the virtual fields method to mechanical characterization of elastomeric materials

Nattawit Promma, Bumedijen Raka, Michel Grediac, Evelyne Toussaint, Jean-Benoit Le Cam, Xavier Balandraud, François Hild

Application of the virtual fields method to mechanical characterization of elastomeric materials

N. Promma [a], B. Raka [b], M. Grédiac [a−*], E. Toussaint [a], J.-B. Le Cam [a]
X. Balandraud [a], F. Hild [b]

September 12, 2008

[a] *Laboratoire de Mécanique et Ingénieries*
Institut Français de Mécanique Avancée-Université Blaise Pascal Clermont II
Campus des Cézeaux. BP 265
63175 Aubière Cedex, France

[b] *Laboratoire de Mécanique et Technologie*
ENS Cachan/CNRS UMR 8535/Université Paris 6/PRES UniverSud Paris
61 avenue du Président Wilson
F-94235 Cachan Cedex, France

[*] *corresponding author, Michel.Grediac@univ-bpclermont.fr*

Keywords

Full-Field Measurements, Hyperelasticity, Image Correlation, Inverse Problem, Large Deformations, Mechanical Characterization, Virtual Fields Method

Abstract

This paper deals with the identification of constitutive parameters of a Mooney model suitable for hyperelastic materials. These parameters are retrieved from a multiaxial mechanical test that gives rise to heterogeneous stress / strain fields. Since no analytical relationship is available between measurements and unknown parameters, a suitable tool, namely the virtual fields method, is developed in case of large deformations and used to identify these unknowns. Several results obtained with numerical simulations and experiments performed on rubber specimens illustrate the approach.

1 Introduction

Modeling the mechanical response of elastomeric materials is commonly carried out within the framework of hyperelasticity (Ward and Hadley, 1993; Holzapfel, 2000). This framework is used as a first approximation, with the restriction that it only describes rate-independent effects without any hysteresis, in the case of isotropic and incompressible materials. Identifying constitutive parameters that govern such a type of law is classically carried out with homogeneous tests, namely uniaxial tensile extension, pure shear and equibiaxial extension. These three types of loading conditions completely describe the domain of possible loading paths (Ward and Hadley, 1993; G'Sell and Coupard, 1994). It is well known that the values of the constitutive parameters that are identified with those three types of test are generally different in practice (Guo and Sluys , 2006). A trade-off between these three sets of values must therefore be found to obtain parameters that can reasonably be considered as intrinsic.

The aim of the present work is to identify the parameters of a given model from only one single heterogeneous test in which the three different types of strain states exist. In that case, the parameters obtained are directly a weighted average of those that would be obtained from the three different tests described above. The challenge here is in retrieving the parameters in a situation for which no closed-form solution exists for the stress, strain and displacement distributions as functions of the applied load and the material properties. Consequently, inverse techniques have to be used. Among these, the finite element model updating technique (Kavanagh and Clough, 1971; Molimard et al., 2005), the constitutive equation gap method (G. Geymonat and Pagano, 2007; Feissel and Allix, 2007; Latourte et al., 2008), the equilibrium gap method (Claire et al., 2004), the virtual fields method (Grédiac, 1989) and the reciprocity gap method (Ikehata, 1990) are

currently developed. The main features of these different methods are presented in (Avril et al., 2008). The equilibrium gap method has been recently used for identification purposes in case of large deformations on steel (Medda et al., 2007) but the finite element model updating technique is the most commonly used in this case (Genovese et al., 2006; Giton et al., 2006; Drapier and Gaied, 2006). Updating finite element models however entails large numbers of calculations. Another technique is used in the present study, namely, the virtual fields method. This method leads to a direct identification of the constitutive parameters in case of linear elasticity (Grédiac, 1989; Grédiac et al., 2006). The objective of the present paper is to investigate its performance in case of large strains and within the framework of hyperelasticity.

The main features of the virtual fields method and its extension to large deformations are presented in the first part of the paper. Some numerical examples then illustrate the relevance of the approach with a special emphasis on the influence of measurement noise on identified parameters. A biaxial test that gives rise to heterogenous strain fields is finally analyzed. Kinematic fields are provided by an image correlation code suitable for large deformations. Typical displacement / strain fields are shown and results obtained in terms of identified parameters are discussed.

2 The virtual fields method in large deformations

Assuming a plane stress state in a solid, the principle of virtual work (PVW) is written as follows (Holzapfel, 2000)

$$t \times \int_{S_0} \mathbf{\Pi} : \frac{\partial \mathbf{U}^*}{\partial X}\, dS_0 = t \times \int_{\partial S_0} (\mathbf{\Pi}.\mathbf{n}).\mathbf{U}^*\, dl \tag{1}$$

where $\mathbf{\Pi}$ is the first Piola-Kirchhoff (PK1) stress tensor, $\mathbf{U}^*$ a kinematically admissible virtual field, $\mathbf{n}$ the normal to the external boundary where the load is applied, and t the thickness of the solid. $\mathbf{X}$ are the Lagrangian co-ordinates. It must be emphasized that the above equation is valid for *any* admissible virtual field **U***. The virtual fields method consists of two main operations:

1. the first one is to express the stress components (Π_{ij} in the present case) as functions of the strain components by introducing the constitutive equations;

2. the second one is to choose a suitable set of kinematically admissible virtual fields ($\mathbf{U}^*$ in the present case) and to write the PVW with these particular virtual fields. These equations lead to linear systems

if the constitutive equations are linear expressions of the constitutive parameters. Inverting the system provides the unknown parameters in this particular case. For non-linear constitutive equations, a cost function is constructed with the PVW and minimizing this cost function provides the sought parameters.

This approach has been successfully used in many examples dealing with the simple case of infinitesimal strains, either in statics (Grédiac et al., 2003) or in dynamics (Grédiac et al., 1998). The objective here is to adapt the procedure to large deformations and to investigate its performances in that case.
Assuming the material is incompressible, the Cauchy stress tensor σ reads

$$\sigma = -p\mathbf{I} + 2\mathbf{B}\frac{\partial W}{\partial \mathbf{B}} \tag{2}$$

where W is the strain energy and $\mathbf{B}$ the left Cauchy-Green tensor defined by $\mathbf{B} = \mathbf{F}\mathbf{F}^{\mathbf{t}}$, and $\mathbf{F}$ the deformation gradient tensor

$$F_{ij} = \frac{\partial x_i}{\partial X_j} \tag{3}$$

where x and X are the Eulerian and Lagrangian co-ordinates, respectively. Eq. (2) is rewritten in terms of principal stretch ratios λ_i, $i = 1 \cdots 3$. These quantities are defined as the ratio between the current length and the initial length along each principal direction i. They are also equal to the eigen values of $\mathbf{F}$. Thus

$$\sigma_i = -p + \lambda_i \frac{\partial W}{\partial \lambda_i}, i = 1 \cdots 3 \tag{4}$$

The strain energy W depends on the first and second invariants I_1, I_2 of the left Cauchy-Green tensor $\mathbf{B}$ (Holzapfel, 2000). They are written as functions of the principal stretch ratios λ_i

$$\begin{aligned} I_1 &= \lambda_1^2 + \lambda_2^2 + \lambda_3^2 \\ I_2 &= \lambda_1^2\lambda_2^2 + \lambda_2^2\lambda_3^2 + \lambda_3^2\lambda_1^2 \end{aligned} \tag{5}$$

Assuming the material is incompressible, we have $J = det\mathbf{F} = \lambda_1\lambda_2\lambda_3 = 1$ and I_2 can be rewritten as follows

$$I_2 = \lambda_1^2\lambda_2^2\lambda_3^2 \times \left(\frac{1}{\lambda_1^2} + \frac{1}{\lambda_2^2} + \frac{1}{\lambda_3^2}\right) = \frac{1}{\lambda_1^2} + \frac{1}{\lambda_2^2} + \frac{1}{\lambda_3^2} \tag{6}$$

Thus

$$\frac{\partial W}{\partial \lambda_i} = \frac{\partial W}{\partial I_1} \times \frac{\partial I_1}{\partial \lambda_i} + \frac{\partial W}{\partial I_2} \times \frac{\partial I_2}{\partial \lambda_i} \tag{7}$$

with

$$\frac{\partial I_1}{\partial \lambda_i} = 2\lambda_i \quad \text{and} \quad \frac{\partial I_2}{\partial \lambda_i} = -\frac{2}{\lambda_i^3} \tag{8}$$

In the case of Mooney hyperelasticity, the strain energy W reads

$$W = C_1(I_1 - 3) + C_2(I_2 - 3) \tag{9}$$

so that

$$\frac{\partial W}{\partial I_1} = C_1 \quad \text{and} \quad \frac{\partial W}{\partial I_2} = C_2 \tag{10}$$

and the eigen Cauchy stresses become

$$\sigma_i = -p + 2\left(C_1\lambda_i^2 - \frac{C_2}{\lambda_i^2}\right),\ i = 1 \cdots 3 \tag{11}$$

where p is an arbitrary hydrostatic pressure that ensures the material incompressibility (Truesdell and Noll, 1965).

In the case of plane stresses, the principal Cauchy stress σ_3 in direction 3 perpendicular to the 1-2 plane is equal to zero. Thus, p can be determined from Eq. (11) and reads

$$p = 2\left(C_1\lambda_3^2 - \frac{C_2}{\lambda_3^2}\right) \tag{12}$$

It is then possible to obtain the two other principal Cauchy stresses σ_1 and σ_2

$$\sigma_i = 2\left[C_1(\lambda_i^2 - \lambda_3^2) - C_2(\frac{1}{\lambda_i^2} - \frac{1}{\lambda_3^2})\right],\ i = 1, 2 \tag{13}$$

The Cauchy stresses σ_{ij} may be expressed in any $1-2$ basis as functions of the eigen Cauchy stresses σ_1, σ_2 gathered in σ' ($\sigma'_{11} = \sigma_1$, $\sigma'_{22} = \sigma_2$, $\sigma'_{ij} = 0$, $i \neq j$)

$$\sigma_{ij} = P_{ik}P_{jl}\sigma'_{kl} \tag{14}$$

where $\mathbf{P}$ is the transition matrix whose components are those of the principal vectors. The PK1 stress tensor $\mathbf{\Pi}$ is derived from the Cauchy stress tensor σ by using the following expression

$$\mathbf{\Pi} = J\sigma\mathbf{F}^{-t} \tag{15}$$

Combining Eqs. (13)-(14)-(15) leads to the first PK1 stresses written as functions of the Mooney parameters C_1, C_2, the principal stretch ratios λ_i, $i = 1 \cdots 3$, the gradient tensor components and the transition matrix components

$$\mathbf{\Pi} = C_1\mathbf{\Theta}(\lambda_1, \lambda_2, \lambda_3) + C_2\mathbf{\Lambda}(\lambda_1, \lambda_2, \lambda_3) \tag{16}$$

where $\mathbf{\Theta}$ and $\mathbf{\Lambda}$ are defined in the appendix.

Introducing the above expression in Eq. (1) leads to the following equation

$$C_1 \int_{S_0} \mathbf{\Theta} : \frac{\partial \mathbf{U}^*}{\partial \mathbf{X}} dS_0 + C_2 \int_{S_0} \mathbf{\Lambda} : \frac{\partial \mathbf{U}^*}{\partial \mathbf{X}} dS_0 = \int_{\partial S_0} (\mathbf{\Pi}.\mathbf{n}).\mathbf{U}^* dl \tag{17}$$

It is worth noting that Eq. (17) is a *linear* function of the unknown parameters C_2 and C_1, thus writing this equation with two different virtual fields leads to a linear system of two equations that is invertible if the virtual fields are independent. The choice of the virtual fields is a key issue since the robustness of the method clearly depends on that choice. Determining the best set of virtual fields has been addressed in the case of linear elasticity and small strains (Grédiac et al., 2002; Avril et al., 2004). In these studies, the idea was to choose virtual fields that minimized the effect of measurement noise on the identified parameters. The strategy proposed in Grédiac et al. (2002), which is based on a heuristic method, is used here for the sake of simplicity.

3 Numerical example

3.1 Introduction

The objective here is to illustrate the previous theoretical approach by using numerical simulations to mimic measured displacement fields. The data are provided by the Finite Element (FE) code ANSYS 11.0 (ANSYS

and user's guide, 2008) for which a set of constitutive parameters C_1 and C_2 is chosen. The goal is to retrieve these two parameters by processing the numerical data with the VFM described in Section 2. A two directional "tensile" test performed on a cross-shaped elastomeric specimen is investigated. The shape and dimensions of the specimen are given in Fig. 1. They have been chosen in such a way that heterogeneous strain / stress fields exist within the specimen. Such a specimen can also be tested by using a multiaxial testing machine (Chevalier et al., 2001), as will be shown in Section 4. A white noise has also been added to the numerical data to examine the stability of the identification procedure to measurement uncertainties.

3.2 FE model

A finite element calculation is performed by assuming both plane stress state and material incompressibility. The four-noded PLANE182 ANSYS element is utilized. Reference values for C_1 and C_2 are chosen to be equal to $0.40\ MPa$ and $0.04\ MPa$, respectively. They represent typical values of the parameters to be identified in the case of carbon black filled natural rubber. The mesh is made of 2976 elements and 3125 nodes. An equibiaxial loading is obtained by prescribing the same displacement U on the four branches. Note however that the stress state is not homogeneous, as discussed in Section 3.5. The global or average stretch λ_g is defined by the ratio of the horizontal or vertical length of the deformed specimen ($110\ mm + 2 \times U$) over its initial length ($110\ mm$). Four numerical examples are studied, namely, $\lambda_g = 1.24, 1.40, 1.56$ and 1.72. In the last case, local levels of principal stretch ratio λ reach values up to 2.18. In practice, the integrals in Eq. (17) are discretized. They are computed using a finite sum of products between the gradient tensor components deduced from the FE programme results at each element centre, the virtual strain at the same point and the area of each element.

3.3 Choice of the virtual fields

As explained above, the choice of the virtual fields is a key issue. The virtual field must be kinematically admissible and described by a continuous function. In the present case, the loading is introduced through 4 grips that prescribe the border of the specimen next to the grips to move along a given direction that is either horizontal or vertical. Consequently, the definition of the virtual field has to take into account this feature. It is uneasy to construct a virtual field defined with the same function over the whole specimen. It has therefore been decided to construct this field piecewise, using a set of 12 rectangular subregions shown in Fig. 1. In

each of these subregions, the virtual displacement field is constructed using shape functions similar to those used in four-noded quadrangular finite elements (Zienkiewicz, 1977). As a result, the virtual displacement within each of these subregions depends of the nodal displacements. It is worth noting that some of the virtual nodes are located outside the central zone of the specimen (*e.g.*, virtual nodes 1, 3, 4, 8, 14, 18, 19, 21 in Fig. 1). This property has no influence on the results since the virtual field is only defined within the central zone of specimen, namely, only the points of the virtual mesh located within this zone influence the calculation of the integrals shown in Eq. (1). Since the virtual fields are kinematically admissible, the "virtual" nodes 1, 2, 3 or 19, 20, 21 in Fig. 1 are subjected to the same vertical virtual displacement. Similarly, nodes 4, 9, 14 or 8, 13, 18 are subjected to the same horizontal virtual displacement. As may be seen in Eq. (1), the external virtual work is an integral of the dot product between the traction and the virtual displacement along the border. If the latter quantity is chosen as a constant, it can be factorized and the integral becomes the resulting load applied to the specimen. This quantity is directly measured by the load cell in practice, thus the external virtual work is easily computed. If non-constant virtual displacements are used along the border of the ROI, this simplification is not possible and the distribution of the traction along this border must be known to be able to compute the external virtual field. This distribution remains however unknown from an experimental point of view. The remaining nodes have no specific constrains. It must also be emphasized that the virtual displacement is continuous from one virtual element to the next whereas the virtual strains are not necessarily. This discontinuity does not induce any error since only the displacement field (and not the strain field) is expected to be continuous to rigorously satisfy the principle of virtual work (Dym and Shames, 1973).

The best set of two virtual fields leading to the two constitutive parameters C_1 and C_2 is obtained as follows. A virtual displacement of each of the virtual nodes lying between some given limits ($\pm 10mm$ in practice) is obtained using the random number generator of Matlab (MATLAB and user's guide, 2008). These displacements are only restricted to satisfy the constraints defined above that ensure the kinematical admissibility of the fields. This procedure is repeated to obtain a second virtual field. Each of the two virtual fields provides a linear equation where C_1 and C_2 are unknown (see Eq. (17)). The independence of the two virtual fields is assessed by computing the condition number of the linear system using the Matlab $rcond$ command. The higher $rcond$, the better the conditioning of the two equations and therefore the lower sensitivity to noise. In practice, several hundreds of sets of virtual fields are tested for each actual field and the virtual fields

leading to the highest condition number are kept for identification purposes. Finding the maximum number of iterations N_{max} used in the heuristic method above is expected to directly influence the value of the maximum $rcond$ number denoted by $rcond_{max}$ in the following. Choosing a high value for N_{max} gives a higher probability of obtaining a large value for $rcond_{max}$, however the computational cost increases. A trade-off between N_{max} and $rcond_{max}$ has been found by progressively increasing N_{max} and noting $rcond_{max}$ in each case. Results found for $\lambda_g = 1.70$ are reported in Table 1. $rcond_{max}$ increases as N_{max} increases, as expected. $N_{max} = 3000$ has been chosen in the present study but it must be pointed out that lower values such as $N_{max} = 500$ or 1000 are also quite acceptable since the condition number only slightly evolves (see Table 1). It is clear that various parameters such as the type constitutive behaviour, the amplitude of the loading, the magnitude of the deformations, the shape of the specimen or the number of experimental points influence the independence of the equations, but this question has not been addressed in the present study.

3.4 Results

The deformed specimen is depicted in Fig. 2 along with the initial shape to illustrate the fact that large strains exist in the sample. This deformed shape corresponds to a global stretch equal to $\lambda_g = 1.72$. Identification results are shown in Table 2. They are very close to the reference values in all cases.

The two virtual fields used to identify the parameters are deduced from the heuristic method described above for each value of the loading level. They lead to two equations whose independence is easily visualized by plotting the corresponding straight lines in the C_1-C_2 plane (see Eq. (17)); the solution being described by the intersection between those lines. Results are shown in Fig. 3. The angle between the two straight lines increases as λ_g increases, thereby meaning that the independence of the equations, and therefore the robustness of the procedure, also increases as the loading level increases. This illustrates the nonlinear response of the material, namely, the heterogeneity of the stress distribution is more important at the last stages of the test, thus the identification is carried out from a wider portion of the σ_i-λ_i curves, $i = 1 \cdots 2$ and retrieving the constitutive parameters becomes easier. A typical set of two optimized virtual fields found for identifying C_1 and C_2 at $\lambda_g = 1.72$ is shown in Fig. 4.

The stability of the method is assessed by adding random noise to the displacements provided by ANSYS. This noise is generated using the Matlab $rand$ function. Its amplitude A_n is equal to 0.022 mm. This

quantity is chosen in such a way that it corresponds to $0.1\ pixel$ for the pictures shot during the experiment presented below. As will be shown, this quantity is of the same order of magnitude as the measurement uncertainty (see Section 4). Twenty independent realizations are considered. The mean value and coefficient of variation of the distribution (defined by the ratio between the standard deviation and the mean value) are reported in Table 3. The scatter decreases as the global stretch λ_g increases since the signal to noise ratio increases. The influence of noise on C_1 is seen to be much less than that on C_2. The influence of each of the two parameters on the mechanical response of the specimen may be assessed by increasing separately each of them by 30% and then by examining the influence of these variations on the $F - \lambda_g$ curve obtained with ANSYS. Results are plotted in Fig. 5, where F is the load applied to each of the four branches. The influence of each of the two parameters is very different, namely, a 30% change in C_1 induces a significant change of force F whereas the same relative variation of C_2 only slightly changes the load response. Parameter C_2 is therefore expected to be identified with a higher uncertainty than C_1, and its sensitivity to noise is higher, as observed in Table 3. Had global measurements (*i.e.*, stroke and load data) only been used, this analysis shows that C_2 would have been very difficult to identify in this particular situation.

3.5 Characterizing the heterogeneity of a test

The virtual fields method is based on the use of heterogeneous actual strain fields. The zone to be analyzed corresponds to the region of interest of the camera in the experiment described in Section 4.1 (Fig. 6-a). The heterogeneity of a given test may be characterized by plotting the distribution of different loading cases in the $I_1 - I_2$ plane. In practice, each finite element centroid provides a point that is plotted in the $I_1 - I_2$ plane. Fig. 6-b shows the distribution obtained for $\lambda_g = 1.72$. The three solid curves correspond to three different basic strain states, namely, equibiaxial tension (ET), uniaxial tension (UT) and pure shear (PS), respectively. The equations of the ET, UT and PS curves are not recalled here, but it has been shown that any stretch state is represented by a point located between the ET and UT curves (G'Sell and Coupard, 1994). For an equibiaxial loading condition, it is observed that the points derived from the FE calculation are located along a certain curve. It has been checked that several points are nearly superimposed on the ET curve, as expected.

Fig. 6-c shows the stretch states as functions of the (X, Y) coordinates in the reference configuration using a suitable color code. The ET, PS and UT states correspond to the blue, green and red colors, respectively.

Intermediate states are defined by a color that is a weighted average of two colors, namely, blue and green for the states between ET and PS, green and red for the states between PS and UT. The weighting is defined using the distance of each point from the curves. Fig. 6-c shows that the central zone of the specimen is mainly in an ET state. The zones corresponding to the four branches are mainly in a UT state. The PS zone is located on a ring-shaped zone located between the ET and UT zones. The heterogeneous character of a test can be also measured by the distribution of the highest stretch ratio λ_{max}. Fig. 6d shows the distribution of λ_{max} with the same color map as before. The lowest and highest values of λ_{max} are respectively equal to 1.26 and 2.18. It is observed that the lowest values of λ_{max} are located in the ET zone whereas the highest values are located in the UT zone. Comparisons with experimental results are presented in next section.

4 Experiments

The objective of this section is to examine the performance of the method by using experimental data. A multiaxial machine is used for stretching a cross-shaped specimen. The displacement fields are measured by using a digital image correlation code.

4.1 Testing machine and sample

The biaxial tests reported herein have been carried out on the multiaxial testing machine ASTRÉE (Fig. 7). Of the six servohydraulic actuators, four of them were displacement-controlled. Consequently, the center of the sample was motionless, which made the displacement measurements easier. External load cells (of capacity equal to 2500 N) were installed. The material considered herein is a carbon black filled natural rubber (34 parts of carbon black per hundred parts of rubber in weight). The actual geometry of the specimen is shown in Figs. 8-9. The total length is $125\ mm$ and its thickness is $2\ mm$. Its central part is a $42 \times 42 mm^2$ square.

4.2 Equibiaxial tests

Specimens are tested under equibiaxial loading conditions (Fig. 8). The maximum global stretch ratio λ_g is equal to 1.70 in both directions. This quantity is very close to $\lambda_g = 1.72$ used in the previous section dealing with numerical simulations. In order to avoid Mullins effects (Mullins, 1948), five loading cycles

are performed prior to testing up to the same value of λ_g in order to stabilize the mechanical response of the specimen. This maximum stretch ratio is obtained in practice by prescribing a displacement to each grip equal to $40\ mm$, with a displacement rate of 0.19 mm/s. Then, measurements are performed during three stabilized mechanical cycles.

4.3 Displacement field measurements

For each loading cycle, forty images are shot by a digital camera (DALSA, resolution: 1024×1024 pixels, dynamic range: 12 bits) located on one side of the specimen. Digital image correlation is performed to measure displacement fields for successive strain states. Such a technique has already been successfully used for measuring large strains while testing elastomeric materials (Chevalier et al., 2001) or glass wool samples (Hild et al., 2002).

A reference picture is considered (Fig. 9). Various interrogation windows (*i.e.*, sub-images or zones of interest (ZOIs)) are considered in the picture. The set of ZOIs defines the region of interest (ROI). Their centers create a measurement mesh. For each interrogation window, the mean displacement is sought by maximizing the cross-correlation of the former with an interrogation window in a picture of the sample in its deformed state. A fast Fourier transform approach is implemented to evaluate the cross-correlation function (Hild et al., 2002). A multiscale algorithm is used to improve the spatial resolution (*i.e.*, to decrease the ZOI size), yet allowing for a large displacement between two consecutive images. The previous approach is recursively applied to images at different scales. First the average strains are deduced from an analysis with images where finer details have been erased. To make the evaluation more robust, the interpolated displacements are applied to the analyzed interrogation window and re-evaluated until the maximum difference between two iterations is less than a chosen value. Details can then be restored in the image (*i.e.*, resolving finer scales) and the displacement interpolation is used as a first evaluation of the field at the new scale. This procedure is iterated until the scale corresponds to the initial ROI (with all its details). During the last step, the displacement is no longer interpolated and fluctuations, whose amplitudes are greater than the ones that are reached with a standard approach, can be analyzed (Hild et al., 2002).

One of the outputs of the correlation code is an estimate of the measurement quality associated with each interrogation window (Hild et al., 2002). It helps the user to control the measurement results. In the present

case, it also enabled us to choose the pictures increment for which the reference image is updated. This choice is particularly important in the present case since very large displacement and strain levels are to be measured. When the reference picture is updated, the measurement uncertainty will increase from analysis to analysis. This effect may induce too low signal to noise ratios. Conversely, if the pictures are not updated, the correlation will eventually fail and no results at all can be used. Therefore, the higher the picture increment, the lower the measurement uncertainty, provided the correlation results are trustworthy. This trade-off was evaluated herein by assessing the performance of the DIC code.

The *a priori* performance of the correlation code is estimated by following the procedure presented in Bergonnier et al. (2005). The central part of the ROI is artificially moved by using the shift / modulation property associated with Fourier transforms. In the present case, a displacement of 0.5 pixel is prescribed along both directions. It was shown that this value leads to the maximum standard uncertainty level (Bergonnier et al., 2005). For an interrogation window size equal to 16 pixels, the standard displacement uncertainty is equal to 0.035 pixel. It is worth remembering that since an updating procedure is used to evaluate large strain levels (Hild et al., 2002), this value is representative of each incremental measurement. As the number of analyzed pictures increases, it is to be expected that the actual measurement uncertainty increases too.

4.4 Results

A typical view of the displacement field obtained when $\lambda_g = 1.70$ is shown in Fig. 10. The central part and the four branches can be clearly distinguished. Differentiating this field provides the four components of the displacement gradient (Figs. 11 and 12). They are obtained by using a centered finite differences scheme. The good quality of the measurements (and of the experiment itself) is highlighted by the two cross-derivatives $\frac{\partial U_1}{\partial X_2}$ and $\frac{\partial U_2}{\partial X_1}$ that are very similar. The gradient components are noisy in Figs. 11-a-c and 12-a-c since the displacement field is not filtered prior to differentiation, contrary to the results shown in Figs. 11-b-d and 12-b-d for which the displacement gradient is derived from displacements smoothed with a 9th degree polynomial fit. The choice of this degree is justified by the fact that the standard deviation between actual and smoothed data is higher for lower values of this degree, but does not significantly evolve when choosing greater values. This assertion is valid for the specific case considered only since no other specimen geometry has been investigated in the present study.

Experimental results are reported in the I_1-I_2 plane (Fig. 13-a). The points are very scattered. The points obtained from smoothed measurements are distributed around the same curve as the one obtained from FE results (see Figs. 13-b and 6-b for comparison purposes). In the same way, the top view of the gauge section as well as the maximum stretch ratio distribution shown in Figs. 13-c-d-e-f are very similar to their numerical counterparts (Figs. 6-c-d). The patch corresponding to the ET zone is not rigorously a circle. It seems moreover to be wider in the experimental results (Figs. 6-c and 13-c-d). This is probably due to the fact that the border of the specimen cannot be precisely defined, namely, interrogation windows astride the boundary of the specimen are removed, thus leading to a smaller UT zone.

Identification is performed by using the procedure described above with filtered data. In Fig. 14, the virtual mesh used for describing the virtual fields is superimposed with the interrogation windows used by the DIC code and the reference picture of the specimen. This view illustrates the fact that 1033 experimental points are processed in practice for identifying the constitutive parameters. The straight lines corresponding to the optimized virtual fields used in the identification procedure are plotted in Fig. 15 for four different values of λ_g. As expected, the angle between the two lines increases as the load level increases but the angle between those lines is somewhat greater than the angles found with the FE simulations, especially for the last stage of the test (see Fig. 3). The co-ordinates of the intersection between the two lines represent the solution in the C_1-C_2 plane. This point moves towards the lower right-hand corner of the view, thus illustrating the fact that the sought parameters do not remain rigorously constant during the test and / or the signal to noise ratio evolves. This effect also appears in Fig. 16 where the identified parameters are plotted vs. λ_g. C_1 slightly increases during the test whereas C_2 slightly decreases. Results obtained for the three tests performed on the same sample illustrate the repeatability of the procedure. It is also worthy of emphasis that the scatter is higher at the beginning of the test, for the lowest values of λ_g. This is certainly due to the fact the heterogeneity of the stress distribution is lower than for higher values of λ_g, so it is more difficult to retrieve accurate values of the identified parameters in this case. This scatter is taken into account for the calculation of the average values of the parameters denoted $\bar{C}_1$ and $\bar{C}_2$. These quantities are defined by

$$\bar{C}_i = \frac{\displaystyle\sum_{j=1}^{n_t} \left(\frac{\lambda_{g_j} - 1}{\sqrt{stdx2_{ij} + stdy2_{ij}}} \right) \times C_{ij}}{\displaystyle\sum_{j=1}^{n} \left(\frac{\lambda_{g_j} - 1}{\sqrt{stdx2_{ij} + stdy2_{ij}}} \right)} \tag{18}$$

where $stdx_{ij}$ ($stdy_{ij}$ respectively) is the standard deviation of the difference between raw and smoothed u_x (u_y respectively) distributions, $i = 1 \cdots 2$, $j = 1 \cdots n_t$, where n_t is the number of images. The higher scatter in the displacement field for a given stretch ratio, the lower confidence in the experimental results. The$\bar{C}_1$ and $\bar{C}_2$ values are reported in Table 4. The $\bar{C}_2$ values are more scattered than the $\bar{C}_1$ values. This is certainly due to their lower contribution to the global mechanical response of the specimens. The values obtained are very close to the classical values of these parameters for this type of material. The beneficial effect of smoothing the u_x and u_y fields can finally be illustrated as follows. Applying the complete identification procedure with raw data (as shown in Figs. 11a-c- and 12a-c-), instead of smoothed data, leads to$\bar{C}_1$ values which remain reasonable: 0.51 MPa, 0.56 MPa and 0.51 MPa for the three tests respectively. $\bar{C}_2$ becomes however much lower than with smoothed data: 0.041 MPa, -0.050 MPa and 0.001 MPa, but the negative value for $\bar{C}_2$ is not admissible (Ball, 1977).

5 Conclusion

The extension of the virtual fields method from small to large deformations is addressed in this paper in case of hyperelasticity. A linear equation is established between parameters governing the Mooney model, actual stretch ratio distribution within the specimen and virtual fields. This equation is written with different virtual fields that are optimized with respect to their independence. This independence is assessed with the condition number, which is related to the stability of the identified parameters when dealing with noisy data. This finally leads to a linear system that provides the unknown parameters after inversion. Numerical simulations illustrate the feasibility and the robustness of the method.

Experiments were then carried out on a cross-shaped rubber specimen. Strain fields are deduced from displacements provided by a digital image correlation system whose measurement quality is discussed in this particular case of large deformations. Results obtained are in agreement with theoretical and numerical expectations, thus confirming the feasibility of the present approach. The identification of parameters governing other types of hyperelastic models will be addressed in the near future.

Acknowledgements

The support of this research by the ”Agence Nationale pour la Recherche” is gratefully acknowledged (PHOTOFIT project).

Appendix

$\boldsymbol{\Theta}$ is defined as follows

$$\begin{cases} \Theta_{11} = \frac{2}{D}\left[(\lambda_1^2-\lambda_3^2)(P_{11}^2F_{22}-P_{11}P_{21}F_{12})+(\lambda_2^2-\lambda_3^2)(P_{12}^2F_{22}-P_{12}P_{22}F_{12})\right] \\ \Theta_{12} = \frac{2}{D}\left[(\lambda_1^2-\lambda_3^2)(-P_{11}^2F_{21}+P_{11}P_{21}F_{11})+(\lambda_2^2-\lambda_3^2)(-P_{12}^2F_{21}+P_{12}P_{22}F_{11})\right] \\ \Theta_{21} = \frac{2}{D}\left[(\lambda_1^2-\lambda_3^2)(-P_{21}^2F_{12}+P_{11}P_{21}F_{22})+(\lambda_2^2-\lambda_3^2)(-P_{22}^2F_{12}+P_{12}P_{22}F_{22})\right] \\ \Theta_{22} = \frac{2}{D}\left[(\lambda_1^2-\lambda_3^2)(-P_{11}P_{21}F_{21}+P_{12}^2F_{11})+(\lambda_2^2-\lambda_3^2)(-P_{12}P_{22}F_{21}+P_{22}^2F_{11})\right] \end{cases} \tag{19}$$

with

$$D = F_{11}F_{22} - F_{21}F_{12} \tag{20}$$

$\boldsymbol{\Lambda}$ is defined as follows

$$\begin{cases} \Lambda_{11} = -\frac{2}{D}\left[(\frac{1}{\lambda_1^2}-\frac{1}{\lambda_3^2})(P_{11}^2F_{22}-P_{11}P_{21}F_{12})+(\frac{1}{\lambda_2^2}-\frac{1}{\lambda_3^2})(P_{12}^2F_{22}-P_{12}P_{22}F_{12})\right] \\ \Lambda_{12} = -\frac{2}{D}\left[(\frac{1}{\lambda_1^2}-\frac{1}{\lambda_3^2})(-P_{11}^2F_{21}+P_{11}P_{21}F_{11})+(\frac{1}{\lambda_2^2}-\frac{1}{\lambda_3^2})(-P_{12}^2F_{21}+P_{12}P_{22}F_{11})\right] \\ \Lambda_{21} = -\frac{2}{D}\left[(\frac{1}{\lambda_1^2}-\frac{1}{\lambda_3^2})(-P_{21}^2F_{12}+P_{11}P_{21}F_{22})+(\frac{1}{\lambda_2^2}-\frac{1}{\lambda_3^2})(-P_{22}^2F_{12}+P_{12}P_{22}F_{22})\right] \\ \Lambda_{22} = -\frac{2}{D}\left[(\frac{1}{\lambda_1^2}-\frac{1}{\lambda_3^2})(-P_{11}P_{21}F_{21}+P_{12}^2F_{11})+(\frac{1}{\lambda_2^2}-\frac{1}{\lambda_3^2})(-P_{12}P_{22}F_{21}+P_{22}^2F_{11})\right] \end{cases} \tag{21}$$

References

ANSYS user's guide, 2008.

Avril, S., Bonnet, M., Bretelle, A., Hild, F., Ienny, P., Latourte, F., Lemosse, D., Pagano, S., Pagnacco, S., Pierron, F., 2008. Overview of identification methods of mechanical parameters based on full-field measurements. Experimental Mechanics 48(4), 381–402.

Avril, S., Grédiac, M., Pierron, F., 2004. Sensitivity of the virtual fields method to noisy data. Computational Mechanics 34, 439–452.

Ball, J., 1977. Convexity conditions and existence theorems in nonlinear elasticity. Archive for Rational Mechanics and Analysis 63, 337–403.

Bergonnier, S., Hild, F., Roux, S., 2005. Digital image correlation used for mechanical tests on crimped glass wool samples. Journal of Strain Analysis 40, 185–197.

Chevalier, L., Calloch, S., Hild, F., Marco, Y., 2001. Digital image correlation used to analyze the multiaxial behavior of rubber-like materials. European Journal of Mechanics. A-Solids 20 (2), 169–187.

Claire, D., Hild, F., Roux, S., 2004. A finite element formulation to identify damage fields. International Journal for Numerical Methods in Engineering 61, 189–208.

Drapier, S., Gaied, I., 2006. Identification strategy for orthotropic knitted elastomeric fabrics under large biaxial deformations. Inverse problems in Science and Enigineering 15 (8), 871–894.

Dym, C., Shames, I., 1973. Solid Mechanics: a Variational Approach.

Feissel, P., Allix, O., 2007. Modified constitutive relation error identification strategy for transient dynamics with corrupted data: The elastic case. Computer Methods in Applied Mechanics and Engineering 196, 1968–1983.

G. Geymonat, F. H., Pagano, S., 2007. Identification of elastic parameters by displacement field measurement. Comptes Rendus de l'Académie des Sciences 330, 403–408.

Genovese, K., Lamberti, L., Pappalettere, C., 2006. Mechanical characterization of hyperelastic materials with fringe projection and optimization techniques. Optic and Lasers in Engineering 44, 423–442.

Giton, M., Caro-Bretelle, A., Ienny, P., 2006. Hyperelastic behaviour identification by a forward problem resolution: application to a tear test of a silicon-rubber. Strain 2006, 291–297.

Grédiac, M., 1989. Principe des travaux virtuels et identification. principle of virtual work and identification. Comptes Rendus de l'Académie des Sciences, 1–5Gauthier-Villars. In French with abridged English version.

Grédiac, M., Fournier, N., Paris, P.-A., Surrel, Y., 1998. Direct identification of elastic constants of anisotropic plates by modal analysis: experiments and results. Journal of Sound and Vibration 210 (5), 645–659.

Grédiac, M., Pierron, F., Avril, S., Toussaint, E., 2006. The virtual fields method for extracting constitutive parameters from full-field measurements: a review. Strain 42, 233–253.

Grédiac, M., Toussaint, E., Pierron, F., 2002. Special virtual fields for the direct determination of material parameters with the virtual fields method. 1- Principle and definition. International Journal of Solids and Structures 39, 2691–2705.

Grédiac, M., Toussaint, E., Pierron, F., 2003. Special virtual fields for the direct determination of material parameters with the virtual fields method. 3- Application to the bending rigidities of anisotropic plates. International Journal of Solids and Structures 40, 2401–2419.

G'Sell, C., Coupard, A., 1994. Génie Mécanique des caoutchoucs et des élastomères thermoplastiques. Appolor.

Guo, Z., Sluys, L.J., 2006, Application of a new constitutive model for the description of rubber-like materials under monotonic loading. International Journal of Solids and Structures 43(9), 2799–2819.

Hild, F., Raka, B., Baudequin, M., Roux, S., Cantelaube, F., 2002. Multi-scale displacement field measurements of compressed mineral wool samples by digital image correlation. Applied Optics 41 (32), 6815–6828.

Holzapfel, G. A., 2000. Nonlinear Solid Mechanics: A Continuum Approach for Engineering. John Wiley and Sons.

Ikehata, M., 1990. Inversion formulas for the linearized problem for an inverse boundary value problem in elastic prospection. SIAM Journal for Applied Mathematics 50, 1635–1644.

Kavanagh, K. T., Clough, R. W., 1971. Finite element applications in the characterization of elastic solids. International Journal of Solids and Structures 7, 11–23.

Latourte, F., Chrysochoos, A., Pagano, S., Wattrisse, B., 2008. Elastoplastic behavior identification for heterogeneous loadings and materials. Experimental Mechanics. In press.

MATLAB user's guide, 2008. The Mathworks.

Medda, A., Demofonti, G., Roux, S., Hild, F., Bertolino, F., Baldi, A., 2007. Sull'identificazione del comportamento plastico di un'accaio a partire da misure a campo intero ottenute tramite correlazione digitale di immagini. In: Proceedings of the XXXVI Convenio Nazionale, AIAS, in Italian.

Molimard, J., Riche, R. L., Vautrin, A., Lee, J., 2005. Identification of the four orthotropic plate stiffnesses a single open-hole tensile test. Experimental Mechanics 45, 404–411.

Mullins, L., 1948. Effect of stretching on the properties of rubber. Rubber Chemistry Technology 21, 281–300.

Truesdell, C., Noll, W., 1965. The non-linear field theories of Mechanics. Handbuch der Physik, III/3, Springer, Berlin.

Ward, I. M., Hadley, D. W., 1993. An introduction to the mechanical properties of solid polymers. John Wiley and Sons.

Zienkiewicz, O., 1977. The finite element method. MacGraw Hill.

List of Tables

N_{max}	500	1000	3000	6000	10000
$rcond_{max}$	0.1297	0.1486	0.1526	0.1561	0.1752

Table 1: Influence of the number of realizations N_{max} on the condition number $rcond_{max}$, $\lambda_g = 1.70$.

λ_g (-)	1.24	1.40	1.56	1.72
C_1 (MPa)	0.3995	0.3995	0.3996	0.3997
Error (%)	*-0.125*	*-0.125*	*-0.1*	*-0.075*
C_2 (MPa)	0.0405	0.0407	0.0405	0.0403
Error (%)	*+1.25*	*+1.75*	*+1.25*	*+0.75*

Table 2: Identified parameters with reference data.

λ_g (-)	1.24	1.40	1.56	1.72
C_1 (MPa)	0.3994	0.3994	0.3999	0.3999
Coef. Variation (%)	*0.8*	*0.4*	*0.2*	*0.01*
C_2 (MPa)	0.0412	0.0405	0.0403	0.0403
Coef. Variation (%)	*8.1*	*4.4*	*2.0*	*1.2*

Table 3: Identified parameters with noisy data, $A_n = 0.1$ pixel.

	C_1 (MPa)	C_2 (MPa)
test 1	0.411	0.139
test 2	0.416	0.091
test 3	0.428	0.075

Table 4: $\bar{C}_1$ and $\bar{C}_2$ for the three different tests.

List of Figures

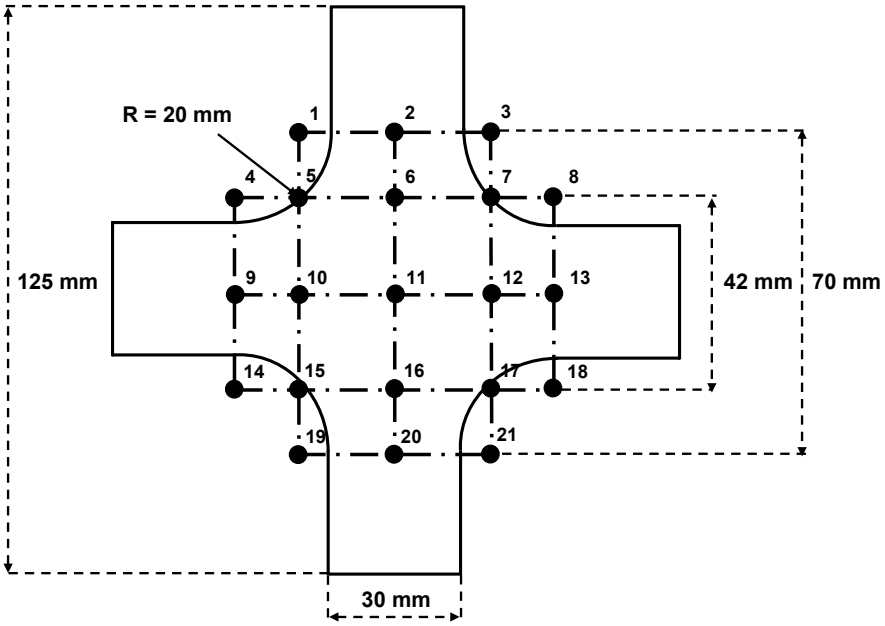

Figure 1: Specimen (solid line) and zones defining the piecewise virtual field (dotted line).

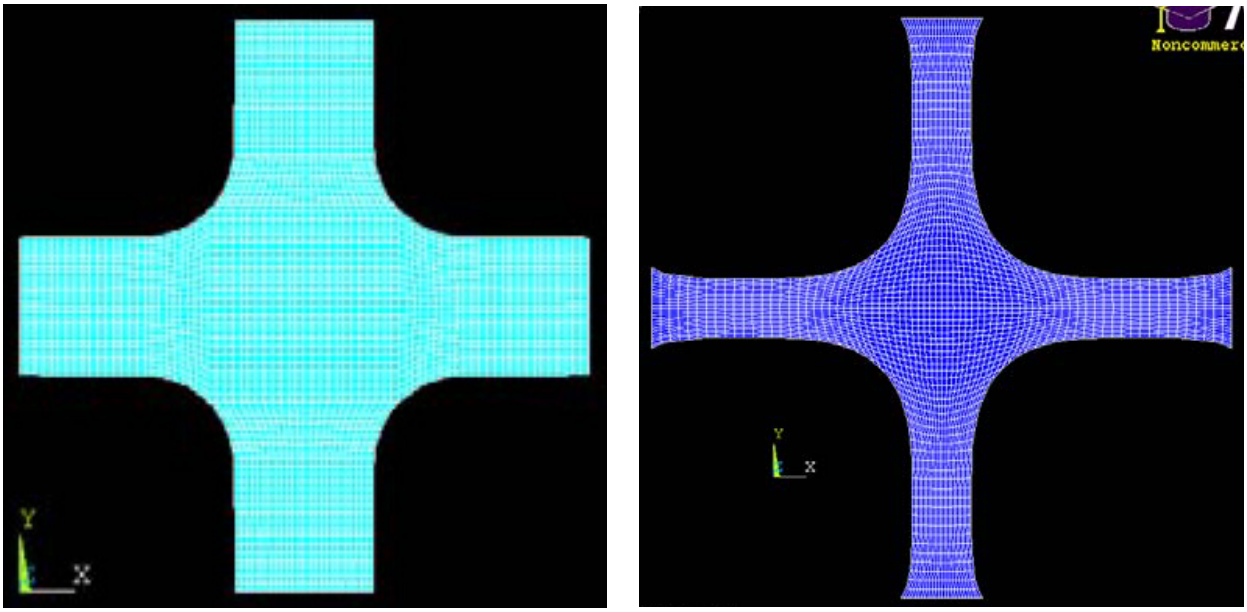

a- undeformed b- deformed, $\lambda_g = 1.72$

Figure 2: Undeformed and deformed states of the studied specimen when $\lambda_g = 1.72$.

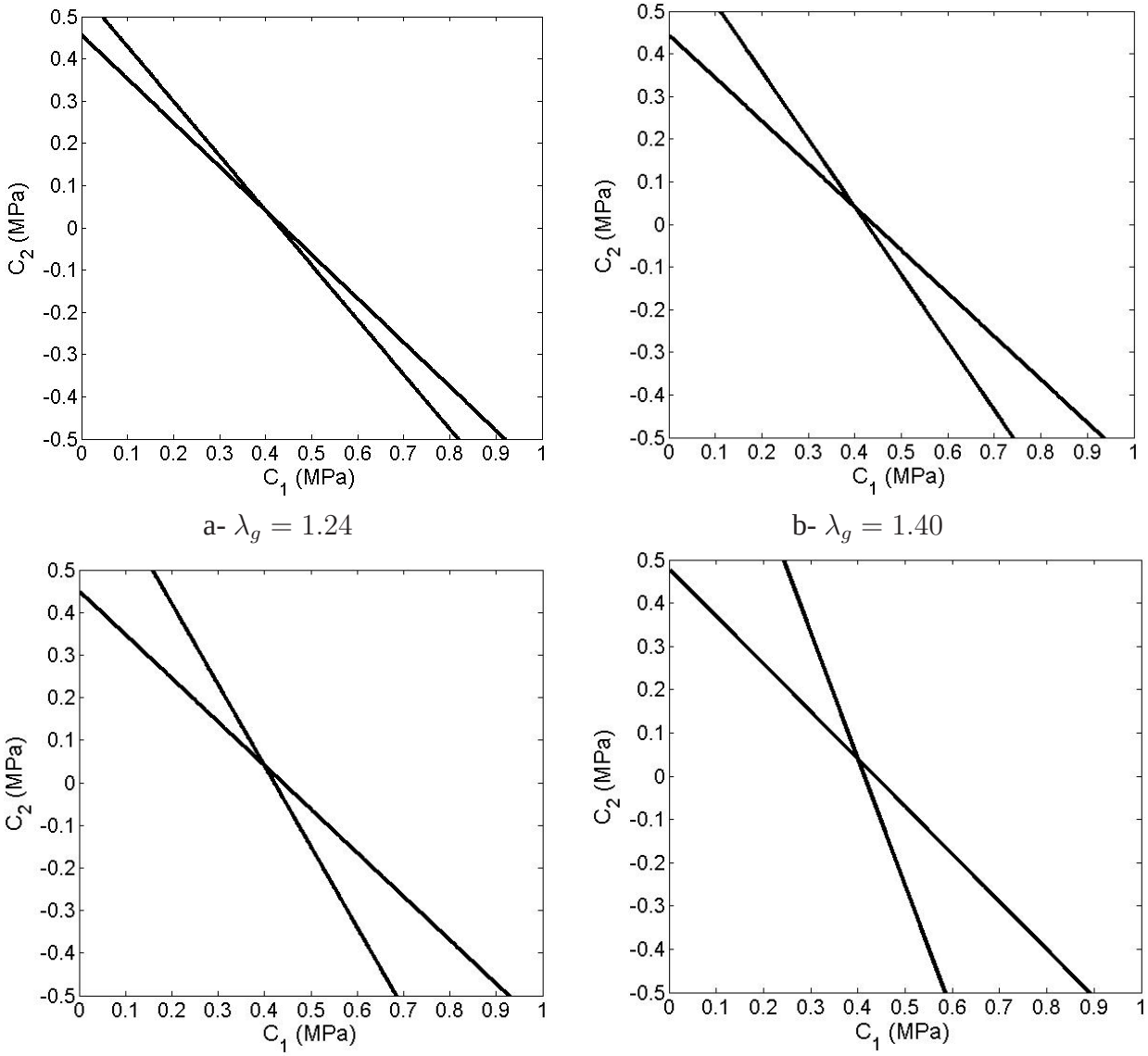

a- $\lambda_g = 1.24$ b- $\lambda_g = 1.40$

c- $\lambda_g = 1.56$ d- $\lambda_g = 1.72$

Figure 3: Straight lines corresponding to various optimized sets of two virtual fields in the C_1-C_2 plane. Their intersection defines the values of the unknown parameters when using simulated data.

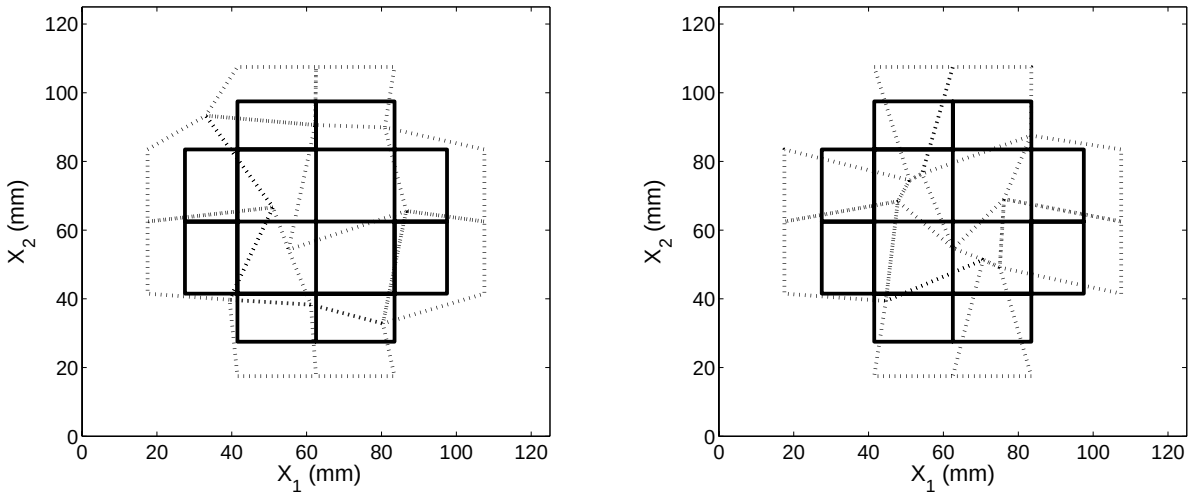

a- Virtual field 1

b- Virtual field 2

Figure 4: Example of two optimized virtual fields (dotted line) used for identifying C_1 and C_2 when $\lambda_g = 1.72$ superimposed with the virtual mesh (solid line).

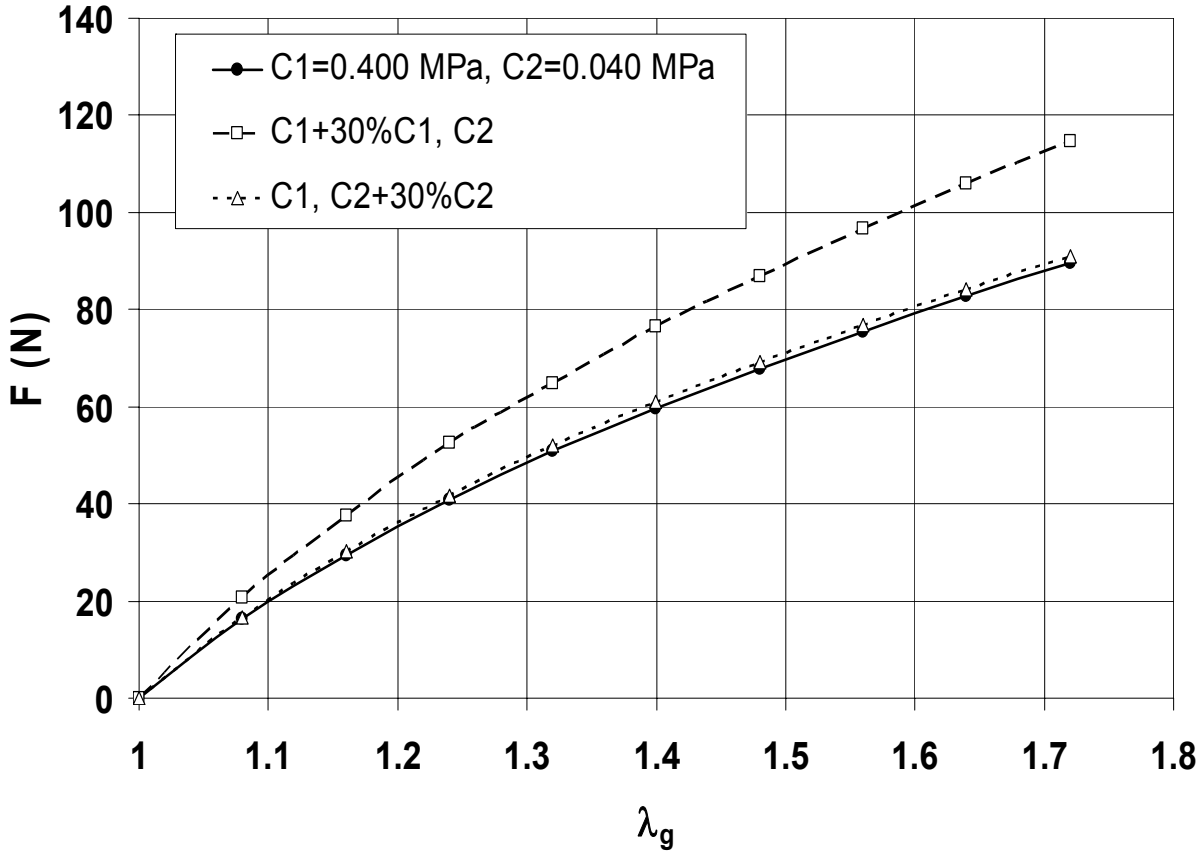

Figure 5: Sensitivity of C_1 and C_2 on the F-λ_g curve when the values of C_1 and C_2 are increased by 30 %.

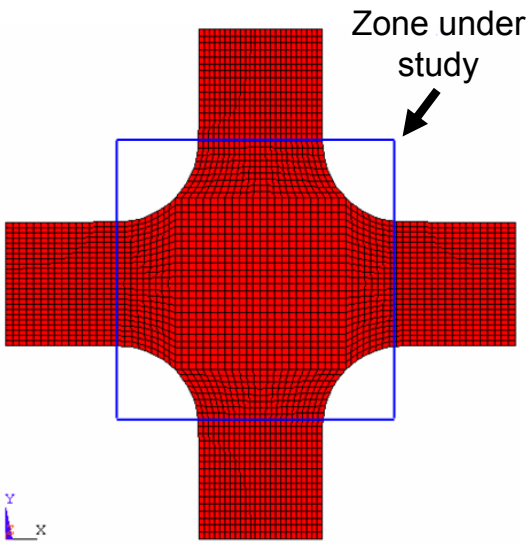

a- Zone under study

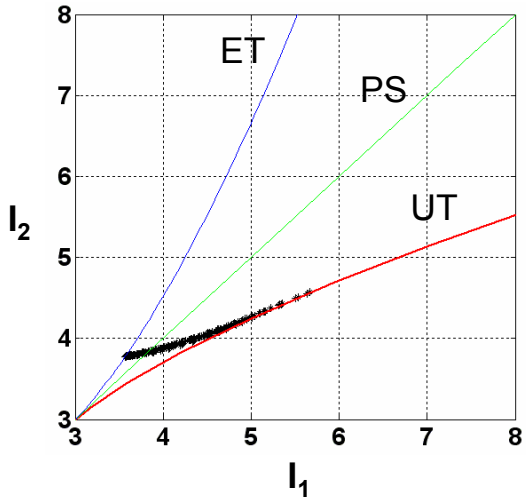

b- Strain state in the I_1-I_2 plane

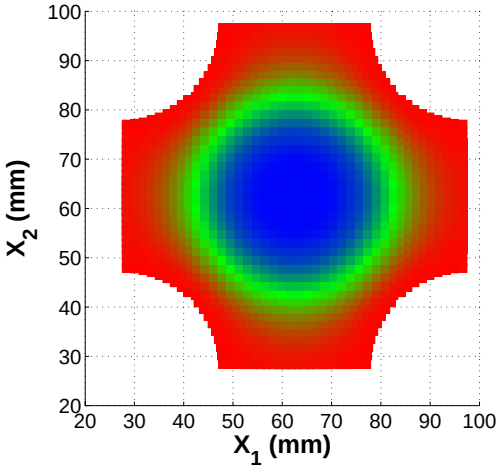

c- Top view of the gauge section

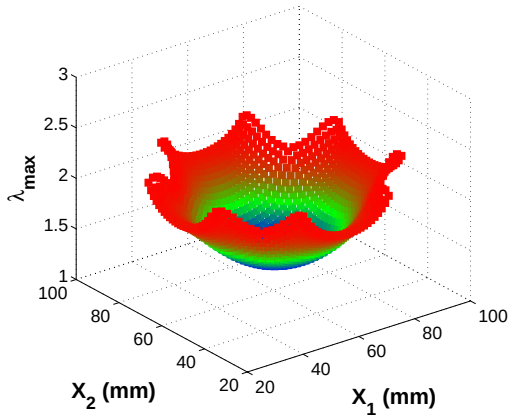

d- Maximum stretch ratio λ_{max} in the gauge section

Figure 6: Numerical simulations

Figure 7: Astrée testing machine

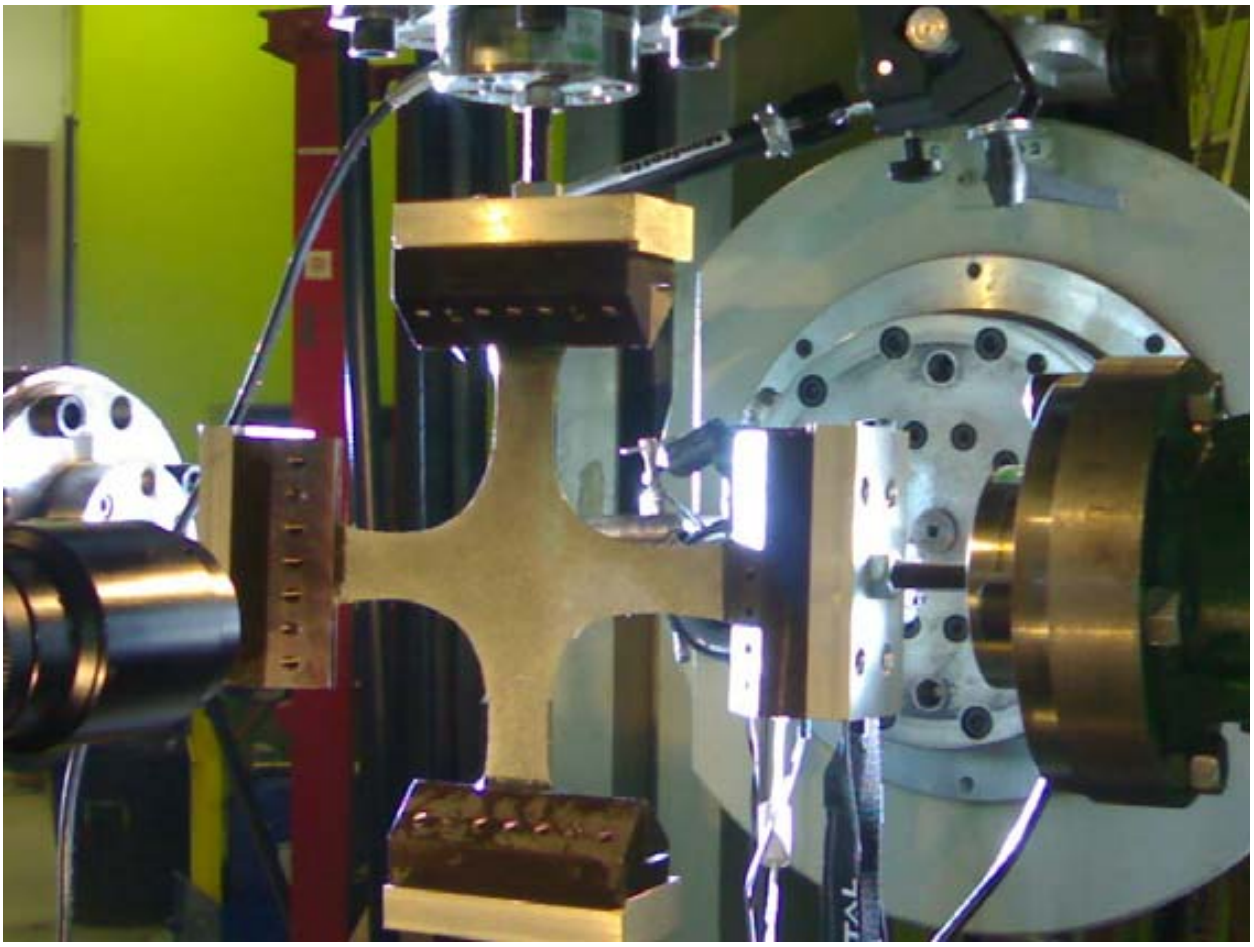

Figure 8: Mechanical setup

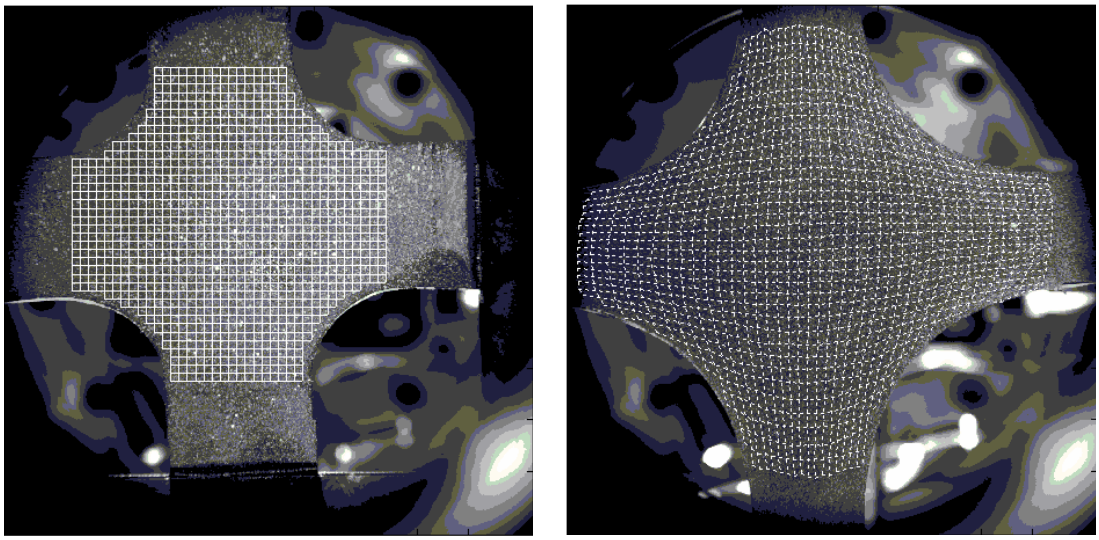

a- $\lambda_g = 0$ b- $\lambda_g = 1.72$

Figure 9: Specimen under test

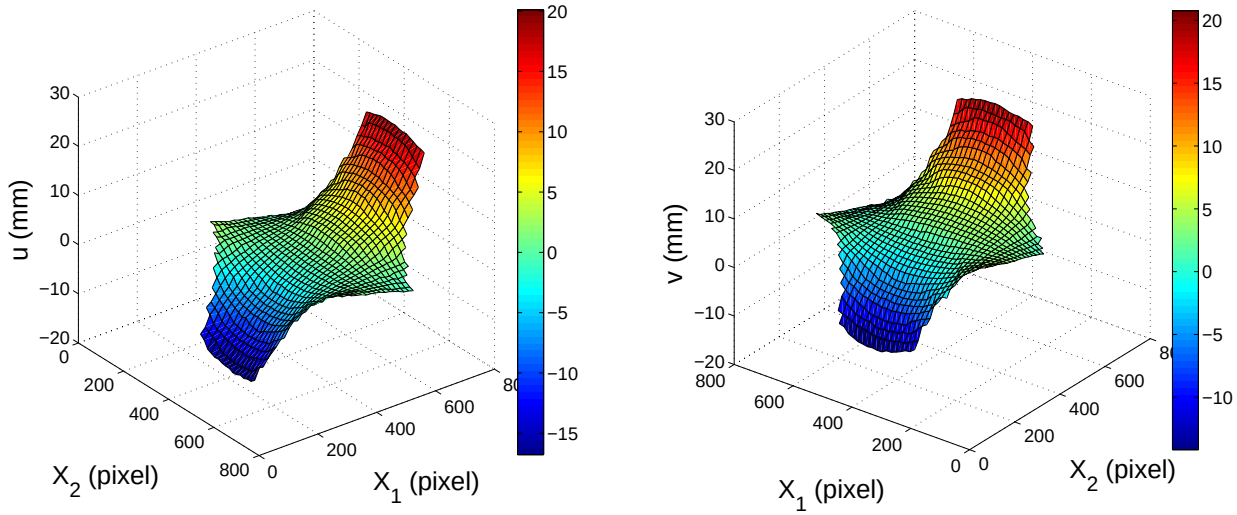

a- u b- v

Figure 10: Displacement field when $\lambda_g = 1.70$

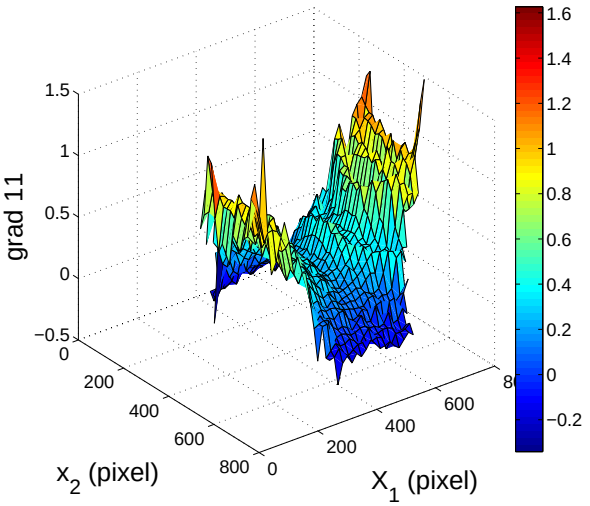

a- $\frac{\partial U_1}{\partial X_1}$

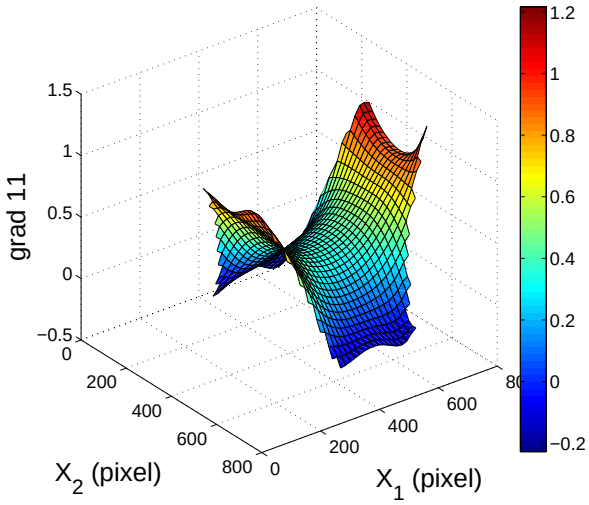

b- $\frac{\partial U_1}{\partial X_1}$, filtered data

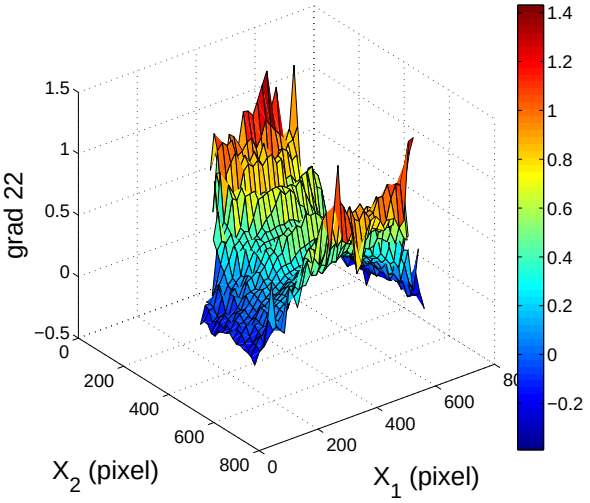

c- $\frac{\partial U_2}{\partial X_2}$

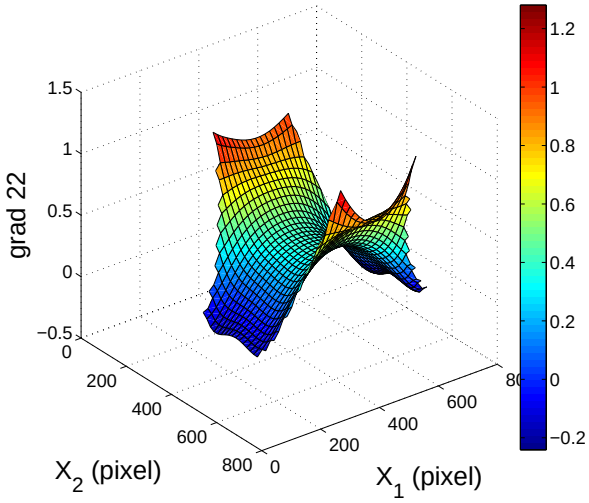

d- $\frac{\partial U_2}{\partial X_2}$, filtered data

Figure 11: Displacement gradient when $\lambda_g = 1.70$. 1/2

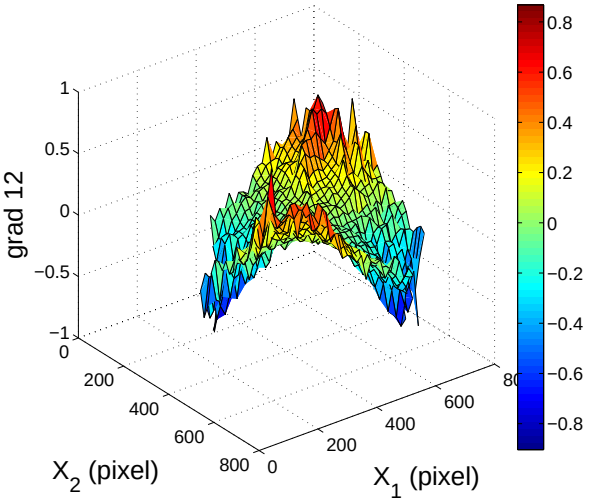

a- $\frac{\partial U_1}{\partial X_2}$

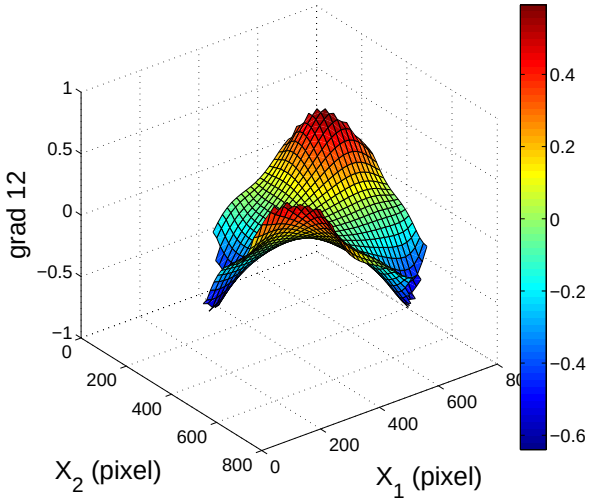

b- $\frac{\partial U_1}{\partial X_2}$, filtered data

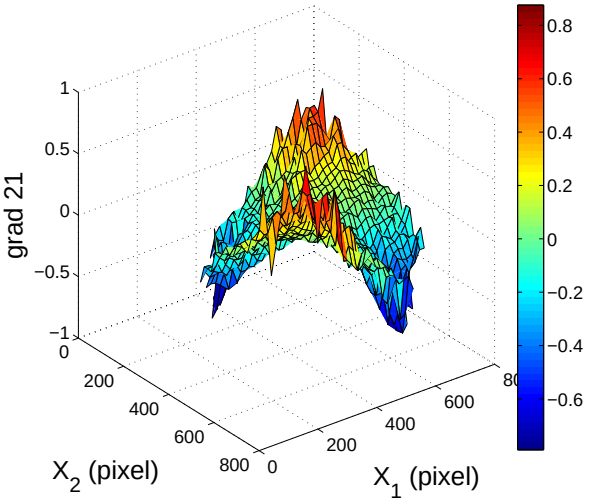

c- $\frac{\partial U_2}{\partial X_1}$

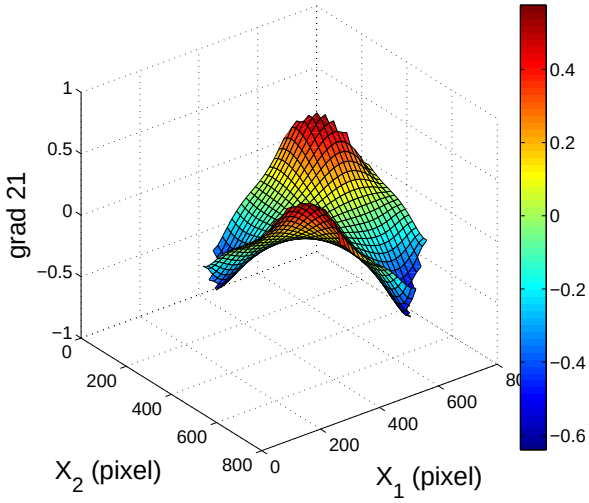

d- $\frac{\partial U_2}{\partial X_1}$, filtered data

Figure 12: Displacement gradient when $\lambda_g = 1.70$. 2/2

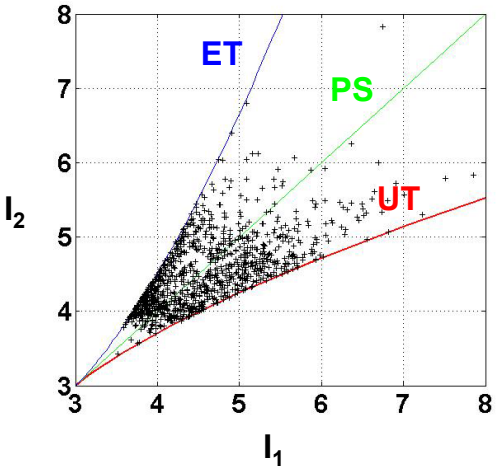

a- Strain state in the I_1-I_2 plane

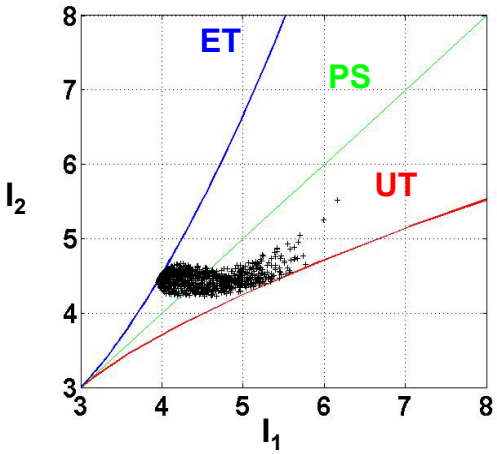

b- Strain state in the I_1-I_2 plane, filtered data

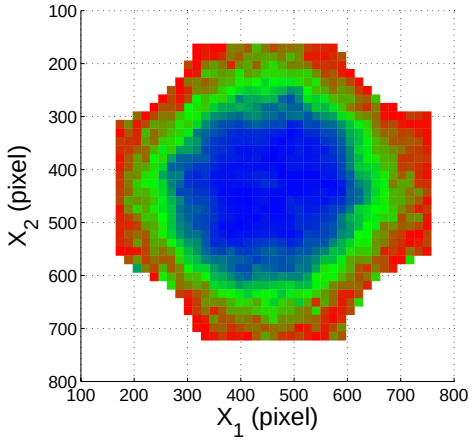

c- Top view of the gauge section

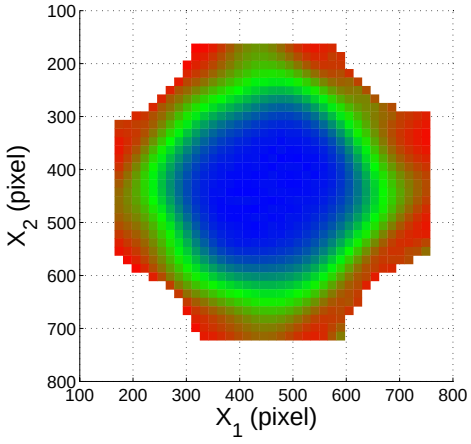

d- Top view of the gauge section, filtered data

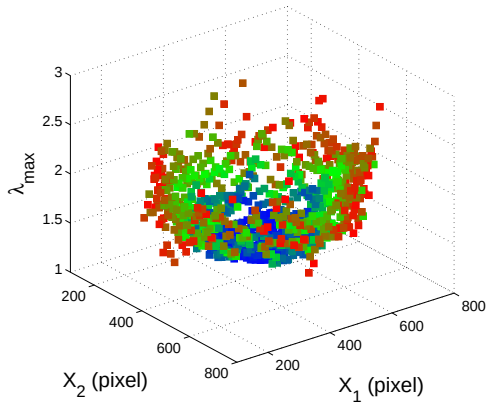

e- Maximum stretch ratio λ_{max} in the gauge section

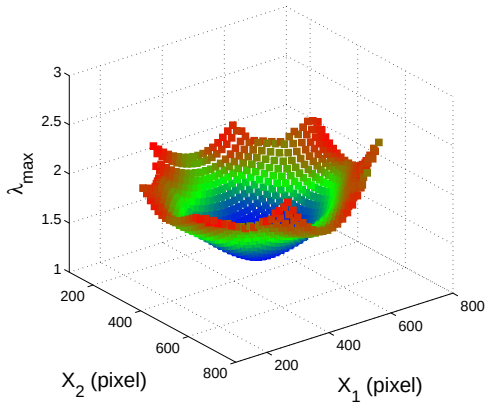

f- Maximum stretch ratio λ_{max} in the gauge section, filtered data

Figure 13: Experimental results

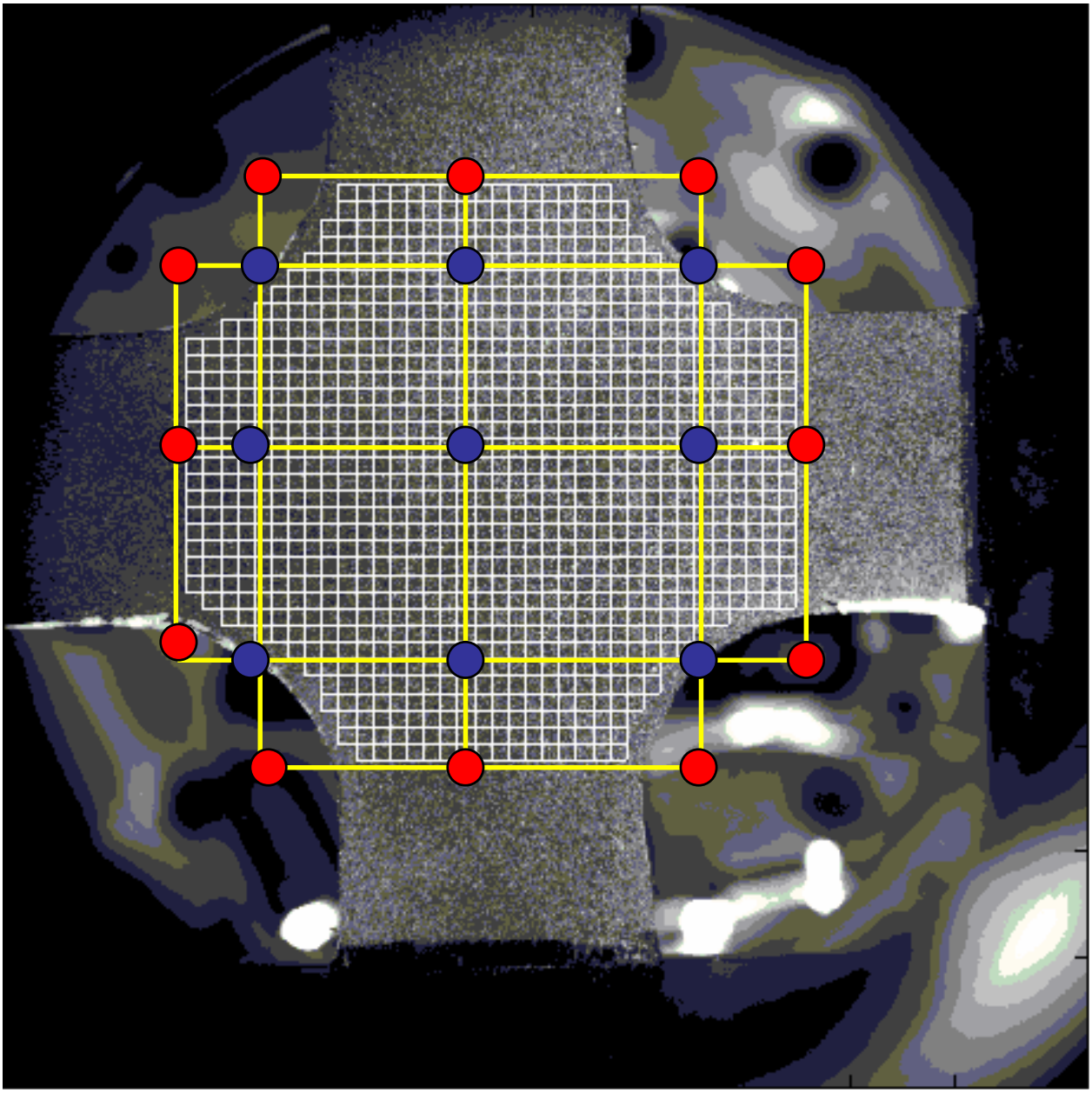

Figure 14: Virtual mesh and specimen under test

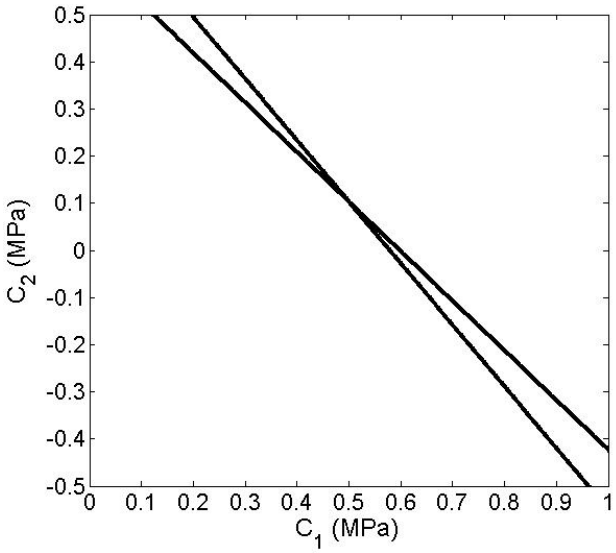

a- $\lambda_g = 1.24$

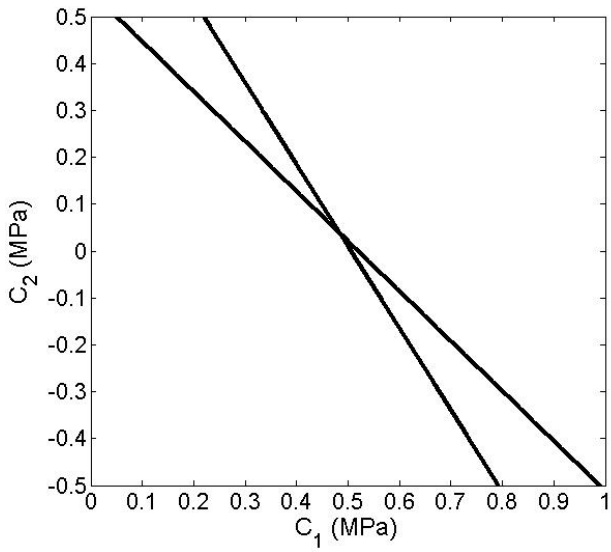

b- $\lambda_g = 1.40$

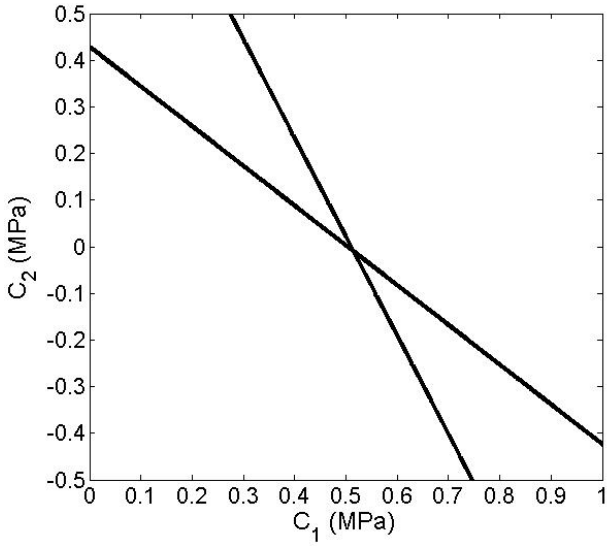

c- $\lambda_g = 1.56$

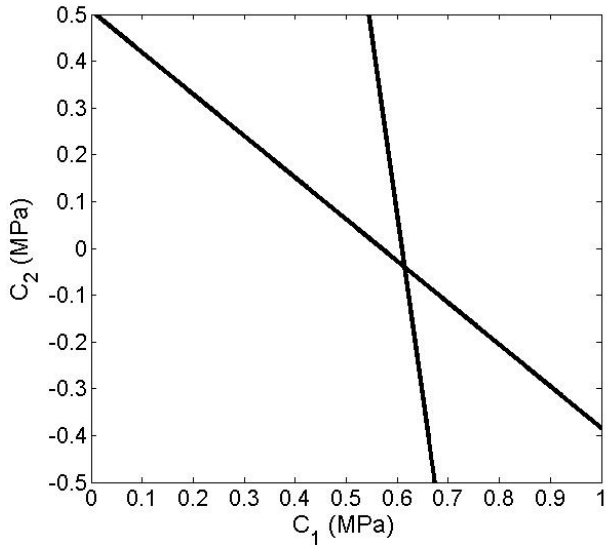

d- $\lambda_g = 1.72$

Figure 15: Straight lines corresponding to various optimized sets of virtual fields in the C_1-C_2 plane, experimental results

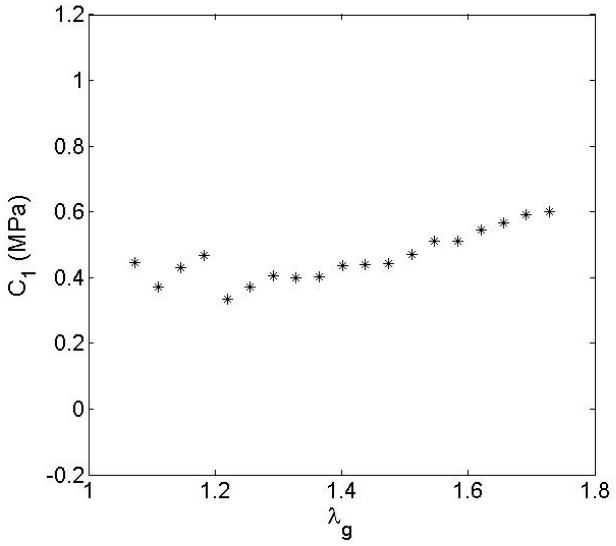

a- C_1, test 1

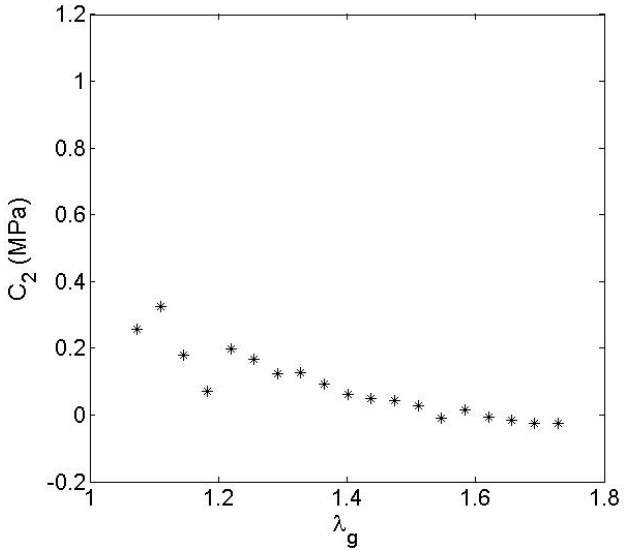

b- C_2, test 1

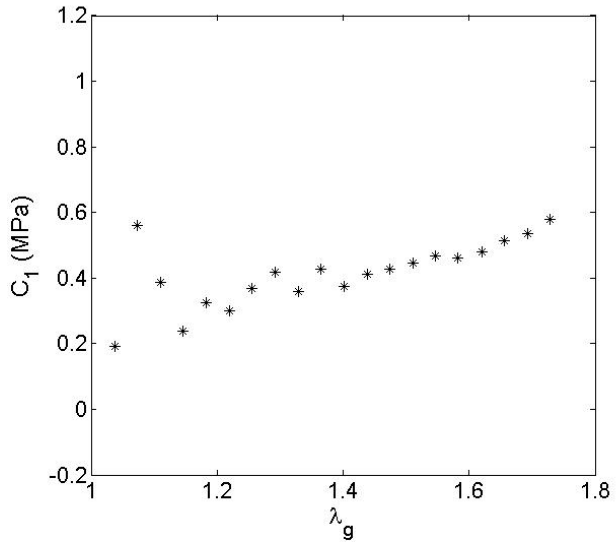

c- C_1, test 2

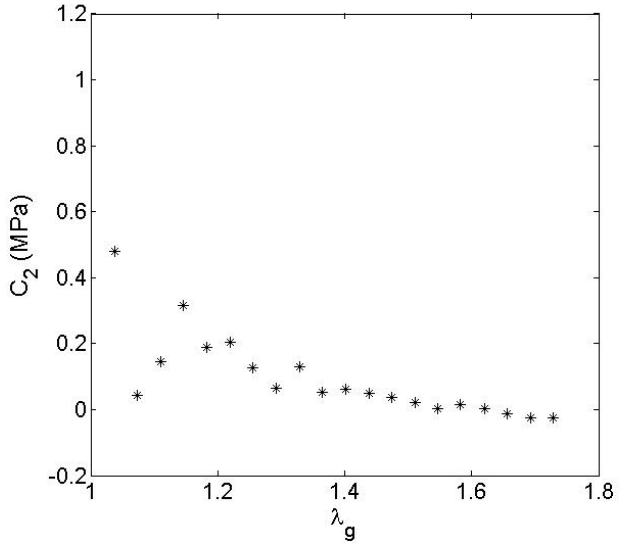

d- C_2, test 2

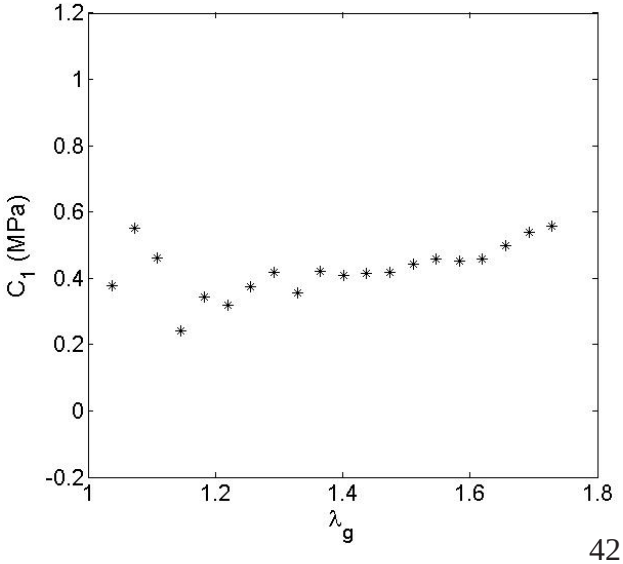

e- C_1, test 3

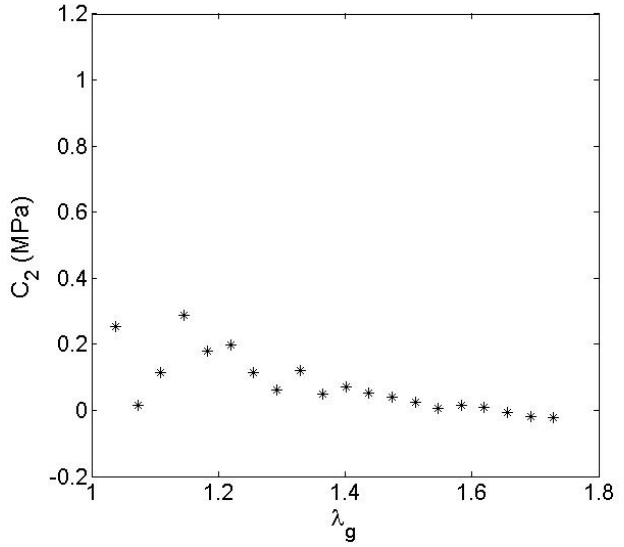

f- C_2, test 3

Figure 16: Identified parameters C_1 C_2 vs. λ_g